Application of 1D paleo-fluvial process modelling at a basin scale to augment sparse borehole data: example of a Permian formation in the Galilee Basin, Australia

Zhenjiao Jiang,[1,2]* Gregoire Mariethoz,[3,4] Matthias Raiber,[5] Wendy Timms[6] and Malcolm Cox[2]

[1] *Key Laboratory of Groundwater Resources and Environment, Ministry of Education, College of Environment and Resources, Jilin University, Changchun, 130021, China*
[2] *School of Earth, Environmental and Biological Sciences, Queensland University of Technology, Brisbane, Queensland, 4001, Australia*
[3] *Institute of Earth Surface Dynamics, University of Lausanne, 1015, Lausanne, Switzerland*
[4] *School of Civil and Environmental Engineering, University of New South Wales, Sydney, New South Walesz, 2052, Australia*
[5] *CSIRO Land and Water, Brisbane, Queensland, 4102, Australia*
[6] *School of Mining Engineering, University of New South Wales, Sydney, New South Wales, 2052, Australia*

Abstract:

The heterogeneous hydraulic conductivity (K) in water-bearing formations controls subsurface flow and solute transport processes. Geostatistical techniques are often employed to characterize the K distribution in space based on the correlation between K measurements. However, at the basin scale, there are often insufficient measurements for inferring the spatial correlation. This is a widespread problem that we address in this study using the example of the Betts Creek Beds (BCB) in the Galilee Basin, Australia. To address the lack of data, we use a 1D stochastic fluvial process-based model (SFPM) to quantify the total sediment thickness, $Z(\mathbf{x})$, and the sandstone proportion over the total thickness, $P_s(\mathbf{x})$, in the BCB. The semivariograms of $Z(\mathbf{x})$ and $P_s(\mathbf{x})$ are then extracted and used in sequential Gaussian simulation to construct the 2D spatial distribution of $Z(\mathbf{x})$ and $P_s(\mathbf{x})$. $P_s(\mathbf{x})$ can be converted to a K distribution based on classical averaging methods. The results demonstrate that the combination of SFPM and geostatistical simulation allows for the evaluation of upscaled K distribution with a limited number of K measurements. Copyright © 2015 John Wiley & Sons, Ltd.

KEY WORDS   heterogeneity; fluvial process-based model; sequential Gaussian simulation; semivariogram

Received 28 March 2015; Accepted 6 November 2015

INTRODUCTION

Groundwater flow and solute transport in aquifers and aquitards are largely controlled by the heterogeneity of hydraulic conductivity (K) (Beckwith *et al.*, 2003; Zinn and Harvey, 2003). In this study, we evaluate the 2D K distribution of the Betts Creek Beds (BCB) in the northern Galilee Basin, Australia, an aquitard that controls the hydraulic connection between the underlying coal beds and the overlying aquifer. Within an area of approximately 74 000 km², there are only 37 values of horizontal K that have been measured in the BCB by drill stem tests in 11 drill holes, and three vertical K values are available. These measurements are insufficient to infer a spatial distribution of K.

Similar problems related to hydraulic conductivity data scarcity are widespread, particularly in basin-scale formations. Several interpolation approaches have been developed over the past several decades to estimate K values (Koltermann and Gorelick, 1996; De Marsily *et al.*, 2005). These methods fall in two broad categories: geostatistical methods, which rely on data to develop a stochastic model of heterogeneity, and process-based methods, which use the knowledge of the physical sedimentary processes. In this paper, we combine aspects of both approaches, by first using a process-based model to generate data, which are then used in a geostatistical context to infer spatial heterogeneity. Before providing details of our approach, we briefly review existing geostatistical and process-based methods.

Kriging estimates the spatial variability of K based on the semivariogram (Journel and Huijbregts, 1978; Deutsch and Journel, 1992). An advantage of kriging is that the estimated K values are conditional to the measured values. However, kriging commonly smooths the estimates of K, which does not reproduce the semivariogram of the data (De Marsily *et al.*, 2005).

Sequential Gaussian simulation (SGS) extends the application of kriging to generate non-smooth heterogeneous

*Correspondence to: Zhenjiao Jiang, Key Laboratory of Groundwater Resources and Environment, Ministry of Education, College of Environment and Resources, Jilin University, Changchun 130 021, China.
E-mail: jiangzhenjiao@hotmail.com

K distributions. The simulation assumes that the local realizations of K follow a Gaussian distribution given by the kriging mean and variance (Goovaerts, 1997). The SGS inherits from kriging the conditioning capabilities and has the advantage of producing interpolations that present a similar spatial variability as observed in the data (Gómez-Hernández and Cassiraga, 1994).

Moreover, in the case of very strong heterogeneity or highly connected patterns, a facies-based model is often used with methods such as object-based models (Coburn *et al.*, 2005), indicator geostatistics (Isaaks, 1984), Markov chains (Carle, 1999; Weissmann and Fogg, 1999) or multiple-point geostatistics (Mariethoz and Lefebvre, 2014).

Most of the geostatistical methods require a sufficient number of lithological data to infer the spatial correlation of the lithofacies. In contrast, process-based models (here the sedimentary processes model) describe the mechanics of sedimentary processes and can simulate the lithological distribution based on scarce lithological logs (e.g. Tetzlaff and Harbaugh, 1989; Paola *et al.*, 1992; Webb and Anderson, 1996). Koltermann and Gorelick (1992), for example, used a process-based model to reproduce the lithological architecture in the Alamenda Creek alluvial fan in California. In their model, river flow and sediment transport, deposition and erosion are simulated over a period of 600 000 years, considering the influence of paleogeography, paleoclimate and paleosediment input on the alluvial processes.

However, there are limitations to the process-based approaches. The lithofacies created by long-term geological processes present uncertainty due to the uncertainty in the parameterization of the sedimentary environment. A method possibly able to quantify this uncertainty is the Monte Carlo simulation, which often requires impractical computation time. Moreover, process-based models are difficult to condition to data (Lopez *et al.*, 2009).

To overcome these limitations, efforts have been made to combine geostatistical methods (which is convenient for data conditioning) and process-based models (which can be used to generate additional realistic data, also called data augmentation) (e.g. Lu *et al.*, 2002; Vargas-Guzmán and Al-Qassab, 2006; Michael *et al.*, 2010; Comunian *et al.*, 2014). For example, Michael *et al.* (2010) used a process-based model to derive statistical attributes, which are then used to simulate the geometry of the deposits with a combination of geostatistical methods. Our approach follows the same logic to characterize the basin-scale heterogeneity of the BCB based on scarce data, with the emphasis on quantifying uncertainties in the BCB thickness and lithological compositions related to the conceptualization of the sedimentary environment.

The process-based model employed here is our recently published method, the stochastic fluvial process-based model (SFPM) (Jiang *et al.*, 2015). It yields the statistics

(mean and variance) of sediment thickness and sandstone proportion, which quantifies the influence of the uncertainty in river discharge, sediment input and riverbed slope on the results. The geostatistical method selected is the SGS, as the architecture of the BCB is sheet-like in geometry and connected channel deposits are not observed (Allen and Fielding, 2007). A two-point geostatistics-based method (SGS) is therefore sufficient to characterize the heterogeneity.

As SGS is a well-established method (Goovaerts, 1997), we here mainly present the application of SFPM to evaluate the distribution of the thickness and sandstone proportion in the BCB and then extract the semivariogram. The study is organized as follows: the Methods section briefly introduces the stochastic fluvial process-based model; the Application to the Betts Creek Beds section describes the geological setting; and the Estimation of Model Parameters section estimates and adjusts the model parameters. Following these sections, SFPM is employed to augment the data and infer the semivariogram in the Results section, and the entire study is summarized in the Conclusion section.

METHODS

The stochastic fluvial process model (SFPM) is employed in this work in order to augment the lithological data. SFPM was recently developed from the convective Exner equation (Paola and Voller, 2005; Davy and Lague, 2009) that describes the mass balance for sediment transport in the river and sediment accumulation on the riverbed (Jiang *et al.*, 2015). SFPM was validated in a local-scale case in Jiang *et al.* (2015), which can also simulate the regional-scale deposition and erosion processes, as there have been several successful applications of the Exner equation at the basin scale (e.g. Heller and Paola, 1992; Koltermann and Gorelick, 1992; Grams *et al.*, 2013). The model can quantify the uncertainties in the sediment thickness and lithofacies related to the paleoflow velocity uncertainty. It consists of solutions for the statistics of sediment load in a river and sediment thickness of the riverbed (details in Jiang *et al.*, 2015), which are briefly summarized in the following discussion.

The statistics (mean and variance) of the sediment load are expressed as

$$\overline{\eta}_m = \sum_{k=1}^{m} \overline{E}_k \frac{\Delta x}{\overline{v}_k} + q_s \left(t - \sum_{k=1}^{m} \frac{\Delta x}{\overline{v}_k} \right) t - \sum_{k=1}^{m} \overline{D}_k \frac{\Delta x}{\overline{v}_k} \quad (1)$$

$$\sigma_{\overline{\eta}_m}^2 = 2x_m{}^2 \left(1 - \frac{x_m + \Delta x}{x_m} e^{-\frac{\Delta x}{x_m}} \right) \left[\sum_{k=1}^{m} \left(\frac{w_{uk}}{\overline{v}_k} \right) \right]^2 \sigma_{v_m}^2 \quad (2)$$

where η is the sediment load in the river (m), m is the index of the node for thickness calculation, k is the index of the

node at upstream of the m node, E is the erosion rate (m/s), D is the deposition rate (m/s), t is the simulation time (s), x is the distance to the river source (m), Δx is the size of discretized segment (m), v is the flow velocity (m/s), w_u is the contribution coefficient of erosion and deposition to the fluctuation of η, q_s is the sediment input from the river source (m), the bar indicates the average, σ^2 represents the variance, both E and D are related to v (Jiang *et al.*, 2015), and q_s is inferred from an empirical equation (Ciesiolka *et al.*, 1995; Guzman *et al.*, 2013):

$$q_s = \varepsilon \cdot Q_0^{0.4} \tag{3}$$

where ε is the sediment transport coefficient, s$^{0.4}$/m$^{0.2}$, Q_0 is the flow rate at the river source, m^3/s.

Equation (1) mathematically describes that η is from the sediment input (q_s) at the river source and the erosion (E) upstream and decreases due to the deposition (D) along the flow path. The sediments deposited in the previous time step can be eroded and deposited further downstream. Equation (2) indicates the impact of velocity uncertainty on σ_η^2 accumulates along the flow path.

The statistics of sediment thickness after a period of Δt are expressed as

$$\overline{Z}_m = \frac{1}{1 - \varphi_m} \left[\overline{D}_m - \overline{E}_m \right] \Delta t, \tag{4}$$

$$\sigma_{Z_m}^2 = \frac{1}{(1 - \phi_m)^2} \left[\left(\frac{\beta_m}{H_m} \right)^2 \sigma_{\eta_m}^2 - 2w_{em} \frac{\beta_m}{H_m} \sigma_{\eta v_m} + w_{em}^2 \sigma_{v_m}^2 \right] \Delta t^2 \tag{5}$$

where Z is the sediment thickness (m), Δt is the magnitude of the time step (s), φ is the porosity of the deposited rocks, H is the depth of the river flow (m), β is the deposition coefficient and w_e is the erosion component in w_u.

Equation (5) provides the fluctuation of the sediment thickness (σ_z^2) in the riverbed as a result of the perturbation of flow velocity ($\sigma_{v_m}^2$) and the induced perturbation of sediment load ($\sigma_{\eta_m}^2$). Both v and η affect Z via the deposition and erosion processes.

Moreover, for the simulation of sand and silt transport, q_s contains both sand and silt with a silt proportion of R_c in the sediment input. The exhausted deposition assumption is widely used in the basin-scale alluvial formation, involving that fine-grain sediments can only be deposited after the coarse-grain sediments are exhausted (Paola *et al.*, 1992).

Based on the exhausted deposition assumption, SFPM yields the means and variances of sandstone thickness (Z_s) and siltstone thickness (Z_c) using Equations (4) and (5). The statistics of the total thickness can be written as

$$\overline{Z}_m = \overline{Z}_{sm} + \overline{Z}_{cm}, \tag{6}$$

$$\sigma_{Z_m}^2 = P_{sm} \sigma_{Z_{sm}}^2 + (1 - P_{sm}) \sigma_{Z_{cm}}^2 \tag{7}$$

where P_s is the sandstone proportion. Z_m is hereafter expressed as $Z(\mathbf{x})$, and $\mathbf{x}$ is the coordinates in the study area. The sandstone proportion (P_s) over the total thickness is defined as

$$P_{sm} = Z_{sm}/Z \tag{8}$$

where P_{sm} hereafter is expressed as $P_s(\mathbf{x})$.

The algorithm of SFPM is summarized in Figure 1, which is implemented in Matlab and is employed to yield the statistics of $Z(\mathbf{x})$ and $P_s(\mathbf{x})$ on a 1D line parallel with the paleoflow direction. The semivariograms of $Z(\mathbf{x})$ and $P_s(\mathbf{x})$ can then be extracted and used in many geostatistical methods to infer the 2D distribution of $Z(\mathbf{x})$ and $P_s(\mathbf{x})$. Here, we use SGS, as an example, which is conducted using Stanford Geostatistical Modeling Software (Remy *et al.*, 2009), and the algorithm can be found in Goovaerts (1997).

Sequential Gaussian simulation results in realizations of $Z(\mathbf{x})$ and $P_s(\mathbf{x})$ on a gridded domain (with the cell size of 3000×4000 m^2 in this study). In each cell of the grid, the vertical lithological architecture is considered as a stack of sandstone and siltstone. The hydraulic conductivities of the sandstone (K_s) and the siltstone (K_c) were measured by field and laboratory tests at centimetre scales (e.g. drill stem tests, slug tests and permeameter). Consequently, the upscaled hydraulic conductivity on
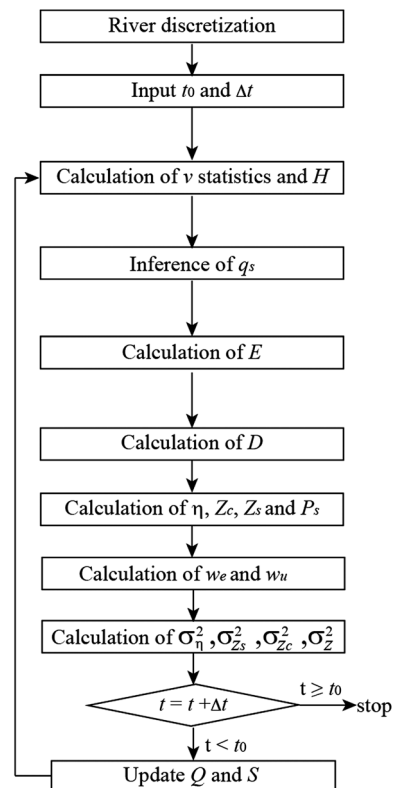

Figure 1. The algorithmic implementation of the stochastic fluvial process model

the gridded domain is calibrated from $P_s(\mathbf{x})$, K_s and K_c, according to the classical averaging methods (Freeze and Cherry, 1977):

$$K_h(\mathbf{x}) = K_s P_s(\mathbf{x}) + K_c[1 - P_s(\mathbf{x})], \qquad (9)$$

$$K_v(\mathbf{x}) = \frac{1}{P_s(\mathbf{x})/K_s + [1 - P_s(\mathbf{x})]/K_c} \qquad (10)$$

where $\mathbf{x}$ is the 2D coordinates in space, K_h is the horizontal hydraulic conductivity (m/d), and K_v is the vertical hydraulic conductivity (m/d).

The 2D horizontal hydraulic conductivity of a formation is often converted to the transmissivity $T(\mathbf{x})$:

$$T(\mathbf{x}) = K_h(\mathbf{x})Z(\mathbf{x}). \qquad (11)$$

There are various methods to upscale the hydraulic conductivity (e.g. Winter and Tartakovsky, 2002; Hristopulos, 2003; Zappa *et al.*, 2006). A simple upscaling method is used here (Equations (9) and (10)) to illustrate the possibility of evaluating the regional-scale distribution of hydraulic conductivity by combining a processes-based model and a geostatistical method. But it is noted that this method may be suboptimal, as the vertical hydraulic conductivity calculation by harmonic mean may overestimate the influence of small K_c, and the influence of boundary conditions on groundwater flow processes is not considered.

APPLICATION TO THE BETTS CREEK BEDS

General geological setting

The northern Galilee Basin in central Queensland, Australia (Figure 2a and b) developed during the Late Carboniferous to Triassic. Stratigraphic formations (Figure 2d) in the basin are divided into two major sedimentary successions according to their depositional environments (Allen and Fielding, 2007). The Joe Joe Group, as the lower succession, is composed of fluvial and lacustrine sediments interbedded with glaciogenic and volcano-lithic beds. Widespread on the top of the Joe Joe Group is the Aramac Coal Measures, which was deposited in peat swamps. After a period of uplift and erosion, the Galilee Basin received deposition of fluvial sediments from the eastern margin of the basin during the Late Permian to the Middle Triassic, which resulted in deposition of the second succession, comprising the BCB, Rewan Formation, Clematis Sandstone and Moolayember Formation (Figure 2d).

During the Late Triassic, an east–west compressional episode resulted in the uplift, folding and partial erosion of the Moolayember Formation, prior to the formation of the overlying Eromanga Basin (Evans, 1980; Hawkins and Green, 1993; Jones and Fielding, 2008), which is a sub-basin of the Great Artesian Basin (GAB). The GAB also includes the formations above the BCB in the Galilee Basin and hosts major aquifers such as the Clematis Sandstone, Hutton Sandstone and Hooray Sandstone (Figure 2d).

The Aramac Coal Measures in the Galilee Basin are considered as a potential target for coal seam gas production. In a natural setting, coal seam gas is entrapped in the coal seams under high pressure. In order to release the gas, groundwater is often extracted from the coal bed to lower the hydraulic pressure in the coal (Morin, 2005). This could affect the groundwater resources in the GAB aquifers due to leakage through the BCB. For gas production and groundwater management, it is important to understand the hydraulic properties of the BCB and in particular the spatial distribution of $T(\mathbf{x})$ and $K_v(\mathbf{x})$, which are the major controls on leakage.

The Galilee Basin was primarily explored for oil and gas reservoirs rather than for groundwater resources in the past, and therefore the hydraulic conductivity measurements in the BCB are too scarce to directly estimate $T(\mathbf{x})$ and $K_v(\mathbf{x})$ in space (Figure 2c). The auxiliary data that support the evaluation of $T(\mathbf{x})$ and $K_v(\mathbf{x})$ are lithological logs in 32 drill holes in the BCB. However, these logs are still too sparse to infer the lithological information between the drill holes. SFPM is therefore employed to augment the lithological data in the BCB along the direction parallel to the paleoflow. In SFPM, the sedimentary environment is conceptualized based on the lithofacies in the BCB, and tectonic and paleoclimate conditions in the Late Permian when the BCB were created.

Lithofacies in the BCB

The lithofacies of the BCB outcrops have been interpreted as fluvial sediments within an alluvial fan, piedmont and mud-flow deposits (Vine and Paine, 1974). A recent investigation at the northeastern margin of the BCB outcrop categorizes the lithofacies of the BCB into the following: association A consisting of conglomerate, multistorey sandstones, cross-bedded sandstones, interbedded sandstone and siltstone and sandy diamictite that record channel deposition environments, and association B consisting of interlaminated sandstone and siltstone, and shale that recorded flood basin environments (Allen and Fielding, 2007). Furthermore, based on the lithological and geophysical logs for the entire Galilee Basin, Allen and Fielding (2007) suggested that most of lithofacies appearing at the northeastern outcrop are related to the entire Galilee Basin. According to the definitions in Hartley *et al.* (2010), the BCB was formed in several large distributive fluvial systems with the apex–toe distances of 100 to 300 km. Created by multiple westerly
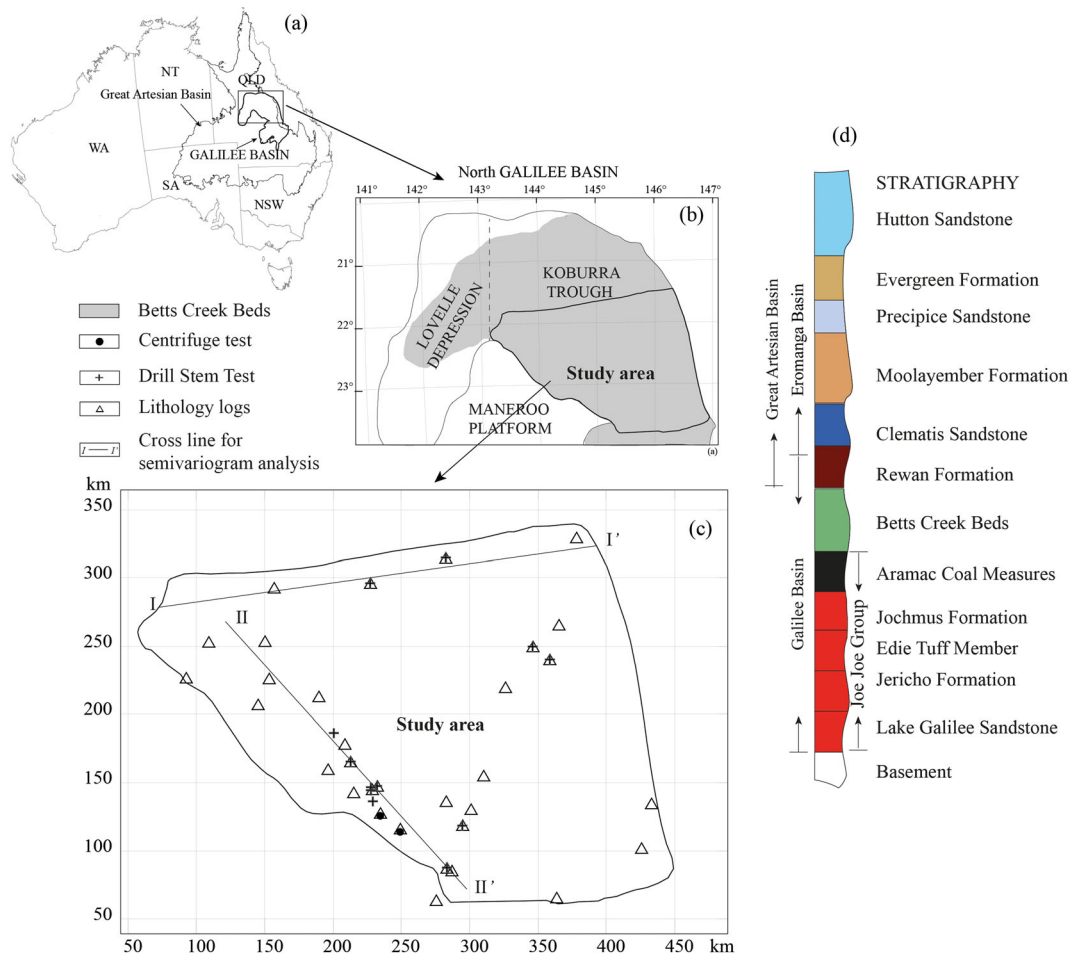
Figure 2. Location map of (a) the Galilee Basin, (b) the north Galilee Basin and the study area, (c) positions of downhole logs (DNRM, http://mines. industry.qld.gov.au/geosciences/geosciences-wireline-log-data.htm), and (d) stratigraphic formations of the Galilee and the overlying Eromanga Basin

and northwesterly flowing meandering and braided rivers with some degree of southward dispersion, BCB lithofacies have a sheet-like geometry in the entire basin.

The extensive sheet-like lithofacies created by river channel migration hide the channel traces. This allows for a spatial stationarity assumption for the river channel positions, implying that as long as the direction of the line selected for 1D SFPM approximately follows the paleoflow direction, the drift between the line and real channel has an insignificant impact on the sedimentation prediction.

The BCB is largely composed of sandstones and fine-grained rocks such as siltstone, claystone and mudstone. Lithofacies are used here to infer the K distribution according to Equations 9–11. K_c were measured for siltstone, claystone and shale using a centrifuge permeameter (method in Timms *et al.*, 2014), and the values do not vary significantly (approximately 5×10^{-7} m/d for three samples). Therefore, SFPM is employed to reproduce two-facies architecture, consisting of sandstone to represent the relatively high-permeability rocks and siltstone to represent the low-permeability rocks.

The deposition period for the BCB is approximately 20 million years. However, sedimentation did not occur continuously because the river can be dry or because erosion and deposition reach a balance. In the absence of dating for the BCB rock samples, the accurate formation period of the BCB is unknown. The simulation period here is assessed according to a global average accumulation rate of fluvial sedimentary basins, which ranges from approximately 0.05 to 10 cm/year (Bridge and Leeder, 1979; Terry *et al.*, 2006). The thickness of the BCB is less than 250 m. We can estimate that over a period of 20 million years, sediment accumulation occurs only in less than 500 000 years (250/0.0005). Hence, modelling a period of 500 000 years is sufficient to simulate the formation of the BCB, assuming that the occurrence of a hiatus did not create widely different landforms that could cause changes of hydraulic conductivity in the BCB.

Tectonics

The northern Galilee Basin contains two depressions, the Koburra Trough and Lovelle Depression, separated by

the Palaeozoic rocks of the Maneroo Platform (Figure 2b). Sediment of the Galilee Basin in this current study area (Figure 2b and c) is confined to the Koburra Trough (Vine, 1973; Hawkins and Green, 1993). The BCB was deposited in almost the entire Koburra Trough (Figure 2b) (Hawkins and Green, 1993). The thermal subsidence and foreland crustal loading provide sufficient accommodation space to preserve the sediments of the BCB (Allen and Fielding, 2007).

The basement topography, on which the BCB was deposited during the Late Permian, is higher in the east and lower in the west. The recent seismic interpretation of structure contours confirms this topography pattern (Van Heeswijck, 1973) and suggests that the slope of the BCB basement is larger in the east and decreases westward, which indicates the sedimentary environments of the BCB varying from hill zones in the east to a plain in the west. Controlled by the basement topography, the majority of the sediment in this study area accumulated in westerly flowing rivers, with the source area in the east margin of the northern Galilee Basin.

Parallel with the dominant paleoflow direction, line I-I′ (Figure 2c) which passes through four drill holes is selected for SFPM. The lithology logs in these drill holes are used for the validation of SFPM. On the line, the distance, x, to the river source is zero at the eastern margin of the Galilee Basin and increases westward to a total distance of 300 km. For modelling, the line is discretized into 1000 segments with Δx of 300 m.

In order to estimate the riverbed slope ($S = dh/dx$), the paleotopography of the BCB basement is fitted by an exponential curve, expressed as

$$h = a \cdot e^{-b\frac{(x-c)}{1000}} - d, \tag{12}$$

where h is elevation (m, Australia Height Datum), a is the intercept (m), b is the coefficient representing the variation rate of the elevation, c is the drift distance (m) and d is used to convert the exponential estimation to the real elevation that can be negative.

In order to infer the coefficients in Equation (12), we convert the coordinates of each drill hole in Figure 2c to the distance from the river source, x. A westward line (such as line I-I′) is used to scan over the study area. When this line passes a drillhole, x for this drillhole is the distance to the eastern margin of the basin along this line.

The elevation (h) of both the top and bottom of the BCB is recorded from the lithological logs, resulting in the scatter map of h versus x (Figure 3). The elevations of both BCB top and bottom indicate similar basement topography. Because d does not affect the calculation of S and v, the selection of d is arbitrary as long as all h can be converted to positive values. Because the smallest elevation read from the lithology logs is −1303 m, we
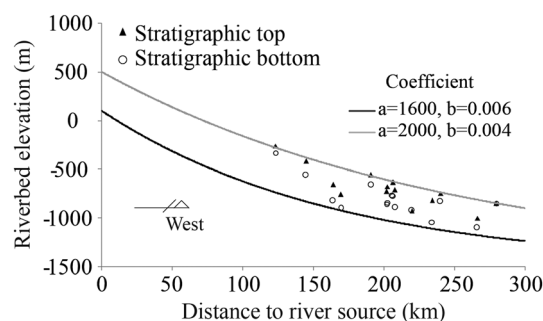

Figure 3. The riverbed topography inferred from the top and bottom of the BCB in the paleoflow direction

use d as 1500 to convert the elevation to $h + 1500$. The exponential relationship in Equation (12) is then used to define two lines that encompass all the data points (Figure 3). As a result, the intercept a at $x = 0$ ranges from 1600 to 2000 m.

Only one of coefficients b and c can be estimated from Figure 3. We assess b in the range of 0.004–0.006, assuming that c is zero. However, the elevation of BCB top and bottom measured today may be different as compared with that in the Late Permian due to post-depositional tectonic movements (such as the landmass rise in the Middle Triassic). Therefore, both b and c will be further adjusted by matching the modelled thickness and lithological composition to the observations from lithological logs (Parameters adjustment section).

Subsidence induces the variation of riverbed topography and the riverbed slope, which can be defined in SFPM as the velocity statistics (Paleoflow velocity section). However, the subsidence rate in the Late Permian is unknown. As the Late Permian is a period of tectonic stability and the subsidence is slow (Hawkins and Green, 1993), the influence of subsidence on the riverbed topography is assumed to be included in the uncertainties of riverbed elevation in Figure 3.

Paleoclimate

The BCB was deposited during the Late Permian (270–250 Ma), at a time when the north Galilee Basin was part of the south-east Gondwana landmass, with latitudes between 40°S to 50°S. According to the paleoclimate simulation based on an atmospheric general circulation model (Fluteau *et al.*, 2001; Roscher *et al.*, 2011), both the temperature and precipitation in the Galilee Basin area in the Late Permian had a seasonal character. Temperature varied from −5 to 30 °C, and the precipitation varied between 1.0 and 7.0 mm/d. This paleoclimate character is comparable with the modern climate of the Canterbury Plains, New Zealand (Wilson, 1985; Soons *et al.*, 2002). Therefore, the sediment coefficients dependent of the climate such as sediment input and composition in the rivers in the Canterbury Plains can be used as a present

analogue to represent the conditions in the Galilee Basin area in the Late Permian (Paleoflow velocity section).

The river discharge (Q) is controlled by the precipitation. The monthly average precipitation in the Thompson River catchment, Queensland, varies from 0.29 to 6.5 mm/d (Bureau of Meteorology, Australia, http://www.bom.gov.au) and has a seasonal character that is comparable with the Galilee Basin area in the Late Permian. Considering the richness of the data, we use Q in the Thompson River from 01/01/1968–31/12/2013 as a present-day analogue. The uncertainties in Q estimates in the Late Permian can be later defined in the statistics of v (Paleoflow velocity section).

Over a period of 16 790 days, there are 10 457 daily Q measurements with 6333 dates missing, and 5254/10 457 of Q measurements are zero (Figure 4a). Daily Q measurements are categorized into 12 monthly bins, and within each month, there are about 870 Q measurements. In each month, Q follows a skewed log-normal distribution (e.g. Figure 4c for February). The monthly Q (averaged over 870 data for each month) follows the seasonal variation, which peaks on February and approaches the lowest value in July (Figure 4b).

ESTIMATION OF MODEL PARAMETERS

Magnitude of time step

Deposition and erosion occur simultaneously; however, the deposition rate (D) relates to sediment load which leads to nonlinear processes of the sediment transport and deposition. To solve this nonlinear problem, we calculate the deposition and erosion sequentially (Figure 1). In order to reduce the error in this calculation, a small time step (Δt) is selected. As shown in Figure 5, when the time step becomes lower than 1.0 day, it has a negligible impact on the result. Therefore, we select the time step as 1.0 day.

Paleoflow velocity

According to Figure 1, v is the key parameter in SFPM determining the sediment transport and accumulation, which is controlled by the paleography and paleoclimate. Following the analysis in the Tectonics and Paleoclimate sections, a Monte Carlo sampling approach is employed to randomly generate h and Q, and produce corresponding realizations of σ_v^2 and $\bar{v}$. The elevation (h) is calculated based on Equation (12), where a is uniformly drawn in the interval 1600–2000 m and b in the interval 0.004–0.006.
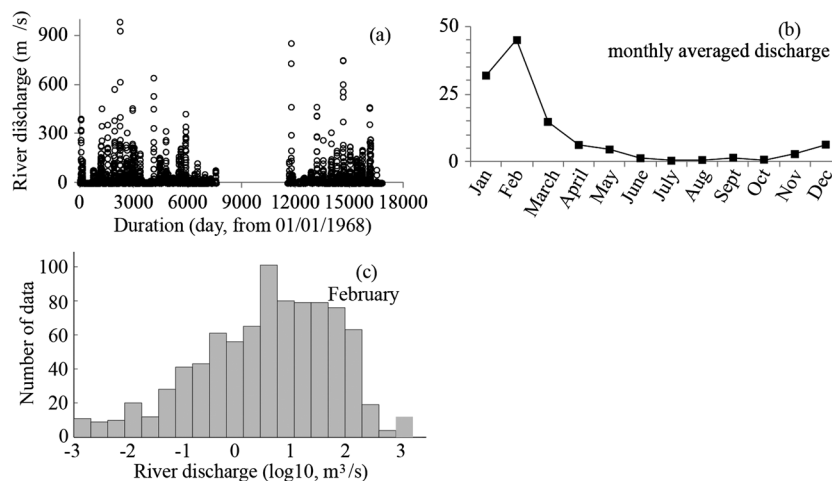

Figure 4. River discharge measured in the Thompson River, Queensland (data from Queensland Department of Natural Resources and Mines database, http://watermonitoring.derm.qld.gov.au/host.htm): (a) the daily observations of Q at the Thompson River, (b) the monthly averaged Q over 46 years and (c) the probability distribution of Q in February
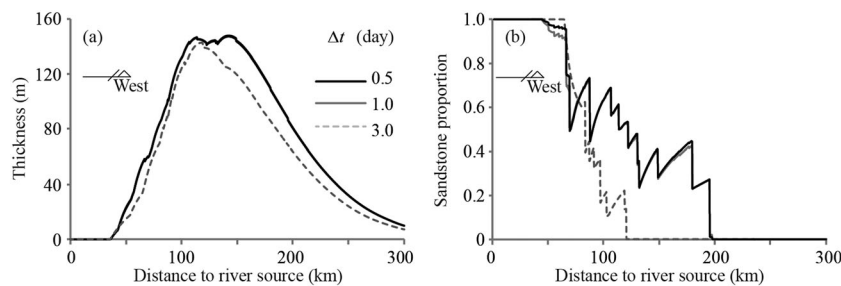

Figure 5. Uncertainty in the (a) modelled thickness and (b) sandstone proportion with different time step magnitudes

To include the seasonal variation of Q in SFPM, Q for each month is randomly generated by the following method: (1) Q for each month are sorted from small to large; (2) the probability corresponding to each value is assigned as $1/N_q$, $2/N_q$, … $(N_q-1)/N_q$, where N_q is the number of Q samples in each month (about 870 values); and (3) a random probability is drawn in [0 1] and the corresponding Q value is selected.

We randomly generated 10 000 realizations of S and Q for each month, which leads to 10 000 v realizations based on the Manning formula (e.g. Le Méhauté, 1976). $\bar{v}$ and are inferred from v realizations for each month (Figure 6a and b).

Spatial variability of $\bar{v}$, σ_v^2 and H in Figure 6b can be fitted by a general equation:

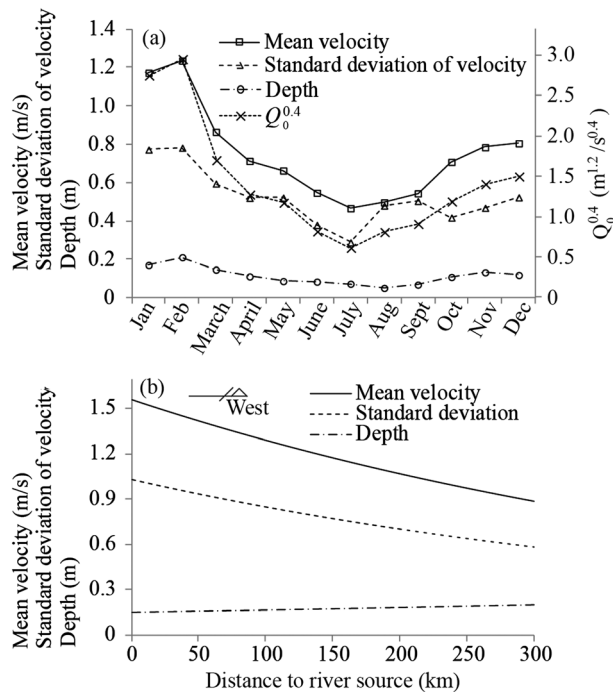$$\mathbf{M} = A_{\mathbf{M}} \cdot \exp[-B_{\mathbf{M}}(x - C)/1000], \qquad (13)$$

Figure 6. Statistics of velocity and river depth: (a) monthly variation of mean and standard deviation of velocity, river depth at $x = 150$ km and the sediments input ($Q^{0.4}$) from the river source, (b) spatial distribution of mean and standard deviation of velocity and river depth in January

with a correlation coefficient of 0.9999–1.0, where $\mathbf{M} = [\bar{v}, \sigma_v^2, H]$ and A, B and C are the coefficients with respect to $\bar{v}$, σ_v^2 and H. Consequently, the spatial distributions of $\bar{v}$, σ_v^2 and H are parameterized as intercept coefficient (A), the curviness coefficient (B) and drift coefficient (C), respectively (Table I).

Comparing Figures 3 and 6b suggests that the spatial distributions of $\bar{v}$, σ_v^2 and H depend on the shape of the riverbed. As mentioned in Equation (12), the drift coefficient (c) is not yet considered. Because both c and C represent the drift of x, which implies that the status of S, $\bar{v}$, σ_v^2 and H at one location is moved to a new location, the adjustment on c is transferable to the adjustment of C. Similarly, B represents the shrinking and expansion of x. Therefore, we can adjust $B_{\bar{v}}$, $B_{\sigma_v^2}$ and B_H uniformly by multiplying a coefficient B_a.

Except for the influences of the flow velocity, the sediment transport and accumulation are affected by q_s and R_c (Methods section). q_s is a function of Q_0 (Equation (3)). The mean of $Q_0^{0.4}$ is estimated from 10 000 Q_0 realizations and plotted in Figure 6a. The constant ε is estimated based on the Selwyn River in the Canterbury Plain, $1.6 \times 10^{-4} s^{0.4}/m^{0.2}$ (with an annual averaged sediment load of 0.00025 m, annual averaged Q is 3.0 m^3/s) (Larned et al., 2008).

Parameters adjustment

C, B_a, ε and R_c here dominate the effects of SFPM, which were estimated according to the present-day analogues earlier. However, these parameters may present uncertainties. It is necessary to adjust them by comparing the modelled $Z(x)$ and $P_s(x)$ and the observations from lithological logs. To adjust these coefficients effectively, the sensitivities of $Z(\mathbf{x})$ and $P_s(\mathbf{x})$ to C, B_a, ε and R_c are analysed by varying one coefficient while freezing all others. For each coefficient, ten values are extracted from the variation range indicated in the legend of Figure 7 and are used in the SFPM to generate ten realizations of $Z(\mathbf{x})$ and $P_s(\mathbf{x})$ on 1000 segments. The dependence of $Z(\mathbf{x})$ and $P_s(\mathbf{x})$ to each coefficient is expressed as the coefficient of variation, CV($\mathbf{x}$), which is the ratio between the standard deviation and mean of ten modelled $Z(\mathbf{x})$ and $P_s(\mathbf{x})$, respectively. CV($\mathbf{x}$) on 1000 segments is converted to the cumulative probability. The domain in Figure 7a and b is

Table I. Parameterization of the spatial distribution of $\bar{v}$, σ_v^2 and H

	Jan	Feb	Mar	April	May	June	July	Aug	Sept	Oct	Nov	Dec
$A_{\bar{v}}$	1.553	1.636	1.147	0.946	0.879	0.725	0.618	0.658	0.721	0.939	1.040	1.068
$A_{\sigma_v^2}$	1.057	1.079	0.630	0.480	0.481	0.255	0.147	0.408	0.448	0.310	0.388	0.486
A_H	0.148	0.182	0.127	0.096	0.075	0.073	0.063	0.045	0.060	0.094	0.115	0.103

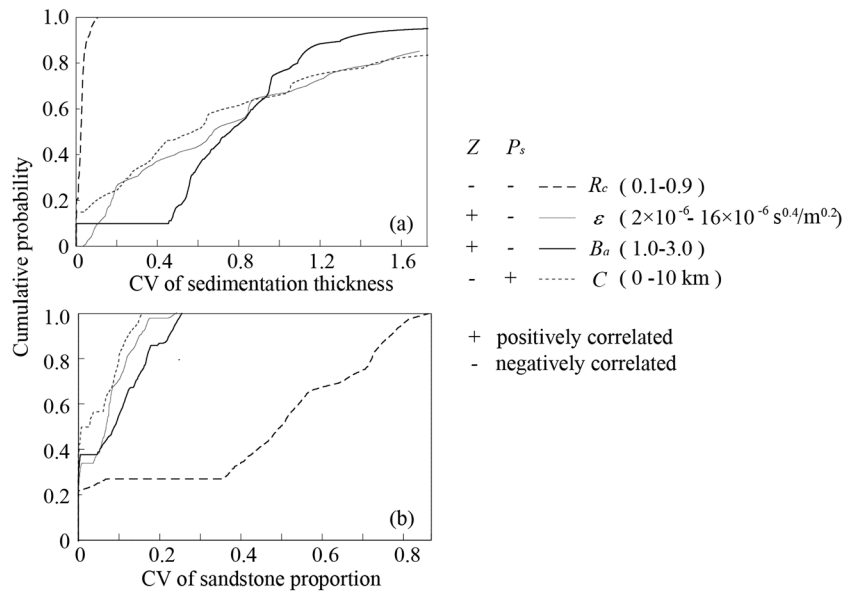$B_{\bar{v}} = 0.002$, $B_{\sigma_v^2} = 0.004$, $B_H = 0.0009$
$C = 0$

Figure 7. Sensitivity analysis of (a) sediment thickness, Z, and (b) sandstone proportion, P_s, due to variation in silt proportion in input sediment (R_c), sediment input volume (ε), velocity curviness (B_a) and velocity drift (C)

divided into upper-left part and lower-right part by the cumulative curves. The smaller area of the upper-left part suggests that CV(**x**) concentrates on the smaller values. In this situation, the dependence of $Z(\mathbf{x})$ or $P_s(\mathbf{x})$ on the investigated coefficient is weaker.

As a consequence, the dependence of $Z(\mathbf{x})$ on the parameters can be sorted as $B_a > \varepsilon > C > R_c$, while the dependence of $P_s(\mathbf{x})$ is as follows: $R_c > B_a > \varepsilon > C$. These orders suggest that $Z(\mathbf{x})$ is mainly affected by the riverbed topography (or paleogeography) and the volume of sediment input from river source, while $P_s(\mathbf{x})$ in a formation is significantly affected by sediment composition in the input sediments from the river source or the upstream.

The correlations between $Z(\mathbf{x})$ or $P_s(\mathbf{x})$ with each coefficient are listed in the right side of Figure 7. As shown, the spatially averaged $Z(\mathbf{x})$ increases with ε and B_a but is reversely related to C. These are attributed to variations in the deposition and erosion processes. An increase in ε means more sediment input into the basin, which leads to an increase in deposition rate and $Z(\mathbf{x})$. An increase in B_a reduces the flow velocity and the erosion rate, therefore, more sediment can be preserved. In contrast, a high C corresponds to the high flow velocity and erosion rate, which induces the loss of sediment from the basin. But $Z(\mathbf{x})$ is weakly affected by R_c.

The spatially averaged $P_S(\mathbf{x})$ is controlled by R_c. The more silts in the input sediment, the less $P_S(\mathbf{x})$. $P_S(\mathbf{x})$ is affected by the other parameters. For example, an increase in C can drive more sands from the upstream to redeposit downstream and results in an increase of $P_s(\mathbf{x})$.

We first adjust C and B_a to alter the spatial distribution of velocity and make the modelled $P_s(\mathbf{x})$ and $Z(\mathbf{x})$

approximately match the observations. ε is then adjusted to mainly fit $Z(\mathbf{x})$, as it has a relatively weak influence on $P_s(\mathbf{x})$. R_c presents a significant control on $P_s(\mathbf{x})$ but has a negligible influence on $Z(\mathbf{x})$, which is finally tuned to fit $P_s(\mathbf{x})$ to the observations.

As a consequence, the modelled $Z(\mathbf{x})$ and $P_s(\mathbf{x})$ match the lithology observations, and the maximum difference between observed and modelled $P_s(\mathbf{x})$ remains under 0.1 (Figure 8b). The adjusted parameters in SFPM are given in the lower-right part in Figure 8, and the statistics of both $Z_s(\mathbf{x})$ and are then calibrated.

Related to the exponential-shape riverbed topography (Figure 3), the flow velocity decreases streamwise. As a result, erosion rate decreases downstream. The deposition rate decreases downstream as well due to the decrease in the sediment load accompanying the deposition processes along the flow path. However, the decreases in the erosion rate and deposition rate play opposite roles. Therefore, a non-monotonic trend on $Z(\mathbf{x})$ appears in Figure 8a, which peaks at 100–200 km from the river source and is reduced both downstream and upstream. $P_s(\mathbf{x})$ generally decreases downstream but with certain fluctuation that is induced by the seasonal variation of sediment input from the river source (Figure 6a).

RESULTS

Semivariogram inference

Both $Z_s(\mathbf{x})$ and $Z_c(\mathbf{x})$ on line *I-I′* follow approximately the normal distributions (e.g. Figure 9). Assuming that the domain is ergodic, a local probability density function for
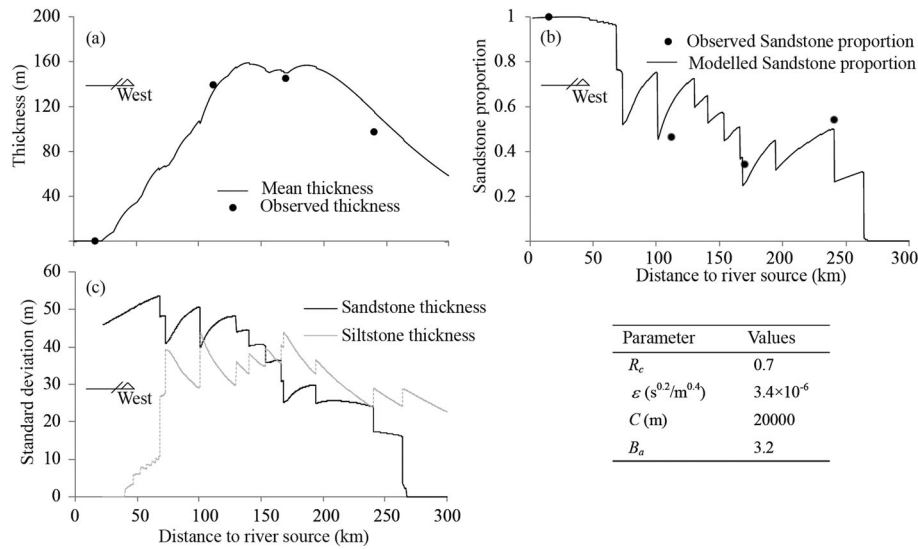
Figure 8. Comparison between modelled results and lithology logs: (a) thickness and (b) sandstone proportion along line *I-I'* to validate the stochastic fluvial process-based model and (c) the standard deviation of sandstone and siltstone thickness relating to the velocity uncertainties
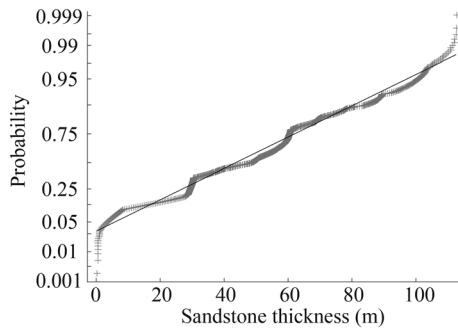

Figure 9. Normality test showing that the spatial variability of the sandstone thickness on line *I-I'* follows the normal distribution

$Z_s(\mathbf{x})$ or $Z_c(\mathbf{x})$ is defined at each segment as a Gaussian of mean $\overline{Z}_s(\mathbf{x})$ or $\overline{Z}_c(\mathbf{x})$ and variance $\sigma^2_{z_s}(\mathbf{x})$ or $\sigma^2_{z_c}(\mathbf{x})$. By drawing values from these local distributions, 100 realizations of $Z_s(\mathbf{x})$ and $Z_c(\mathbf{x})$ are generated on lines *I-I'*. These values are then converted to total thickness $Z(\mathbf{x})$ and sandstone proportion $P_s(\mathbf{x})$, which are used as the basis for the experimental semivariogram inference.

Semivariograms for both $Z(\mathbf{x})$ and $P_s(\mathbf{x})$ are adjusted to fit the resulting 100 experimental semivariograms using the least-squares method (Figure 10a and b). As a result, semivariogram for $Z(\mathbf{x})$ in the paleoflow direction follows a Gaussian model and for $P_s(\mathbf{x})$ follows an exponential model. The semivariogram of $P_s(\mathbf{x})$ increases periodically with a period of about 25 km, which is induced by the fluctuations of P_s in Figure 8b. For robust estimates of P_s at the unmeasured positions, the semivariogram for P_s is constructed at the lag distance smaller than 30 km, and the correlation coefficients of P_s at two positions with the separation distance larger than 30 km is defined as zero.

The variability of $Z(\mathbf{x})$ and $P_s(\mathbf{x})$ may be different in directions parallel and perpendicular to the paleoflow. This difference is quantified as an anisotropy factor, which is the ratio between semivariogram ranges perpendicular and parallel to the paleoflow direction.

In order to estimate this factor, another line (*II-II'*) approximately perpendicular to line *I-I'* is selected such that it passes close to as many drill holes as possible (Figure 2c). The semivariogram values are calculated based on 19 lithological logs near *II-II'*, which lead to a Gaussian model with a range of 90 km and sill of 3300 m² (Figure 10c). Comparison between Figure 10a and c demonstrates a significant nugget effect in the semivariogram on line *I-I'*, which defines the uncertainties in quantifying the paleogeography and paleoclimate by SFPM. Once this nugget effect is removed from the sill on line *I-I'*, the remaining sill values on line *I-I'* and *II-II'* are comparable (which are both around 3000 m²).

The anisotropy factor is then evaluated to be 0.75 (90/120 km). Considering that the nugget on line *II-II'* presents uncertainty, we hereafter use a relatively large nugget (1900 m²) and sill (5200 m²) in the semivariogram in both directions to obtain more variable realizations of the sedimentation thickness.

The lack of data pairs for $P_s(\mathbf{x})$ results in the impossibility to infer a semivariogram. We here assume that the anisotropy factor for $P_s(\mathbf{x})$ is the same as that of $Z(\mathbf{x})$, as both $P_s(\mathbf{x})$ and $Z(\mathbf{x})$ are determined by the spatial variation of $Z_s(\mathbf{x})$ and $Z_c(\mathbf{x})$.

BCB thickness, sandstone proportion and hydraulic conductivity

Once the semivariograms for $P_s(\mathbf{x})$ and $Z(\mathbf{x})$ are determined from the augmented data on line *I-I'*, the 2D
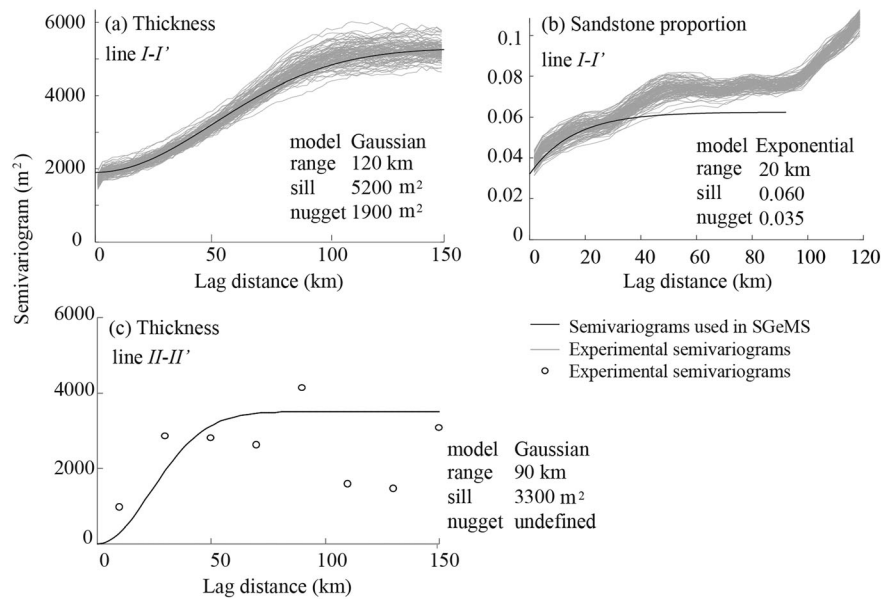
Figure 10. Experimental and modelled semivariograms of (a) thickness and (b) sandstone proportion on line *I-I'*, and (c) thickness semivariogram on line *II-II'*

distributions of $P_s(\mathbf{x})$ and $Z(\mathbf{x})$ can be created by SGS (using Stanford Geostatistical Modeling Software) conditional to the data set from 32 downhole logs. As shown in Figure 11, $Z(\mathbf{x})$ generally increases from east to west, and after peaks in the central part, $Z(\mathbf{x})$ decreases towards west. Within the entire thickness, the high sandstone proportion more likely appears in the east (Figure 11).

Ten possible realizations of $Z(\mathbf{x})$ and $P_s(\mathbf{x})$ were generated and were converted to vertical hydraulic conductivity $K_v(\mathbf{x})$ and transmissivity $T(\mathbf{x})$ using the averaging methods in Equations 9–11. In the averaging method, sandstone hydraulic conductivity (K_s) is inferred from drill stem test, which ranges from 0.01 to 0.1 m/d with an average value of 0.038 m/d (based on 37 sets of drill stem test). Here, we use 0.038 m/d for K_s. The hydraulic conductivity for the low-permeable rocks (K_c) is about 5×10^{-7} m/d.

As a consequence, ten realizations of hydraulic conductivity at the basin scale are evaluated for the

BCB (Figure 12). The spatial variability of K_v appears to be weaker than that of T. This is because the stacked two-layer model (sandstone overlying siltstone) is assumed to convert P_s to the hydraulic conductivity (Equation (10)), where K_v is the harmonic mean of K_s and K_c. As a consequence, K_v is significantly affected by the small value of K_c (5×10^{-7} m/d) rather than the spatial variation of P_s.

A less ideal facies distribution in each cell (more patchy or interfingered, rather than perfectly stacking) would lead to the upscaled K_h and K_v values in 3D grids. However, this is beyond the scope of this study. It is difficult to recreate the lithological sequence accurately in the Late Permian over a period of millions of years by fully considering the sedimentary processes, as the sedimentary environment is too complex to be determined. However, because the total thickness of sandstone and siltstone has been assessed and the spatial structures (semivariograms) of $P_s(\mathbf{x})$ and $Z(\mathbf{x})$ are determined, the lithology architecture
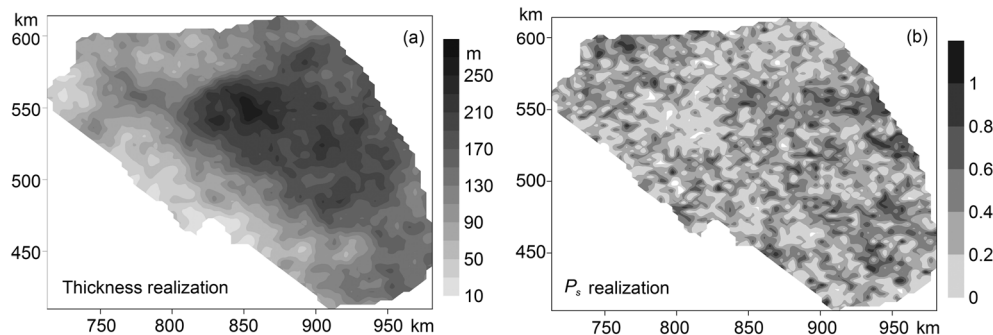

Figure 11. One realization of (a) sediment thickness and (b) sandstone proportion resulting from sequential Gaussian simulation
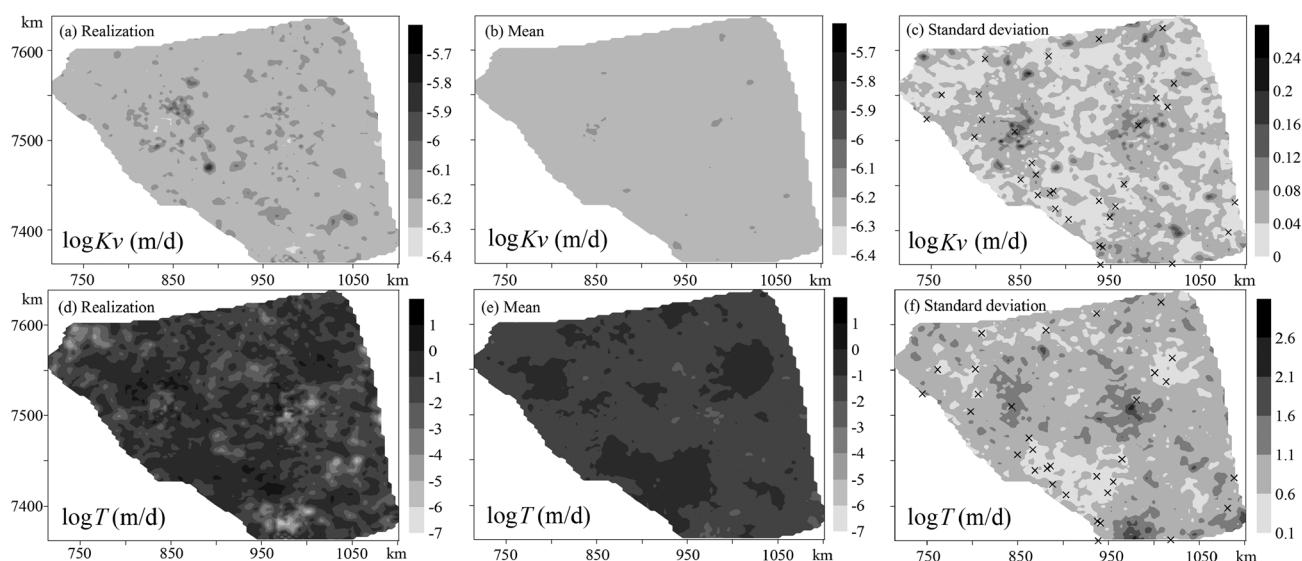
Figure 12. One realization, mean and standard deviation of the realizations. Top row: logarithm of the vertical hydraulic conductivity; bottom row: logarithm transformation of the transmissivity, and (c) and (f) also show the positions of lithological logs

with different degrees of sandstone/siltstone connectivity can be constructed by statistical methods, and the details about how the sandstone and siltstone are interfingered and how the connectivity of sandstone/siltstone affects the hydraulic connection between underlying coal bed and the overlying aquifer will be discussed in the future.

lithological architecture, when hydraulic conductivity measurements are scarce. SFPM augments the lithological data parallel to the paleoflow direction by simulating the sedimentary environment, while the geostatistical method yields the spatial variability of the lithology conditional to lithological data.

CONCLUSION

This study quantifies the heterogeneity of the hydraulic conductivity in the BCB using an SFPM to augment the data. SFPM incorporates the uncertainty related to climate and tectonic factors in the statistics of the flow velocity. It is used to characterize the stochasticity of the lithological profile parallel with paleoflow direction, where the transport and accumulation of sand and silt are simulated. As a result, SFPM provides the variance and mean of the total sediment thickness, as well as the sandstone proportion over that thickness.

Semivariograms are extracted from the simulated thickness and sandstone proportion and are used in SGS to generate the 2D spatial distribution of these variables. The results are then converted to the transmissivity based on the arithmetic averaging and the vertical hydraulic conductivity based on the harmonic averaging. The resulting heterogeneity of the BCB and the quantification of uncertainty constitute a basis for future stochastic modelling of the trends of hydraulic connection between the Aramac Coal Measure and the overlying Great Artesian Basin aquifers at the regional scale.

The process-based model and geostatistical models offer complementary tools to infer the basin-scale hydraulic conductivity distribution via characterization of the

REFERENCES

Allen JP, Fielding CR. 2007. Sedimentology and stratigraphic architecture of the Late Permian Betts Creek Beds, Queensland, Australia. *Sedimentary Geology* **202**: 5–34.

Allen JP, Fielding CR. 2007. Sequence architecture within a low-accommodation setting: an example from the Permian of the Galilee and Bowen basins, Queensland, Australia. *AAPG Bulletin* **91**: 1503–1539.

Beckwith CW, Baird AJ, Heathwaite AL. 2003. Anisotropy and depth-related heterogeneity of hydraulic conductivity in a bog peat. I: laboratory measurements. *Hydrological Processes* **17**: 89–101.

Bridge JS, Leeder MR. 1979. A simulation model of alluvial stratigraphy. *Sedimentology* **26**: 617–644.

Carle SF. 1999. *T-PROGS: Transition Probability Geostatistical Software*. University of California: Davis, CA.

Ciesiolka C, Coughlan K, Rose C, Escalante M, Hashim GM, Paningbatan E Jr, Sombatpanit S. 1995. Methodology for a multi-country study of soil erosion management. *Soil Technology* **8**: 179–192.

Coburn TC, Yarus JM, Chambers RL. 2005. Stochastic modeling and geostatistics: principles, methods, and case studies, vol. II, AAPG computer applications in geology 5. AAPG.

Comunian A, Jha S, Giambastiani BS, Mariethoz G, Kelly BJ. 2014. Training images from process-imitating methods. *Mathematical Geoscience* 46: 241–260.

Davy P, Lague D. 2009. Fluvial erosion/transport equation of landscape evolution models revisited. *Journal of Geophysical Research, Earth Surface 2003–2012* 114: F03007.

De Marsily G, Delay F, Gonçalvès J, Renard P, Teles V, Violette S. 2005. Dealing with spatial heterogeneity. *Hydrogeology Journal* 13: 161–183.

Deutsch CV, Journel AG. 1992. *Geostatistical Software Library and User's Guide*. Oxford university press: New York.

Evans P. 1980. Geology of the Galilee Basin. *The geology and geophysics of northeastern Australia: Geological Society of Australia* 2: 299–305.

Fluteau F, Besse J, Broutin J, Ramstein G. 2001. The Late Permian climate. What can be inferred from climate modelling concerning Pangea scenarios and Hercynian range altitude? *Palaeogeography, Palaeoclimatology, Palaeoecology* 167: 39–71.

Freeze RA, Cherry JA. 1977. *Groundwater*. Prentice-Hall.

Gómez-Hernández JJ, Cassiraga EF. 1994. Theory and practice of sequential simulation. In *Geostatistical Simulations*. Springer Netherlands; 111–124.

Goovaerts P. 1997. *Geostatistics for Natural Resources Evaluation*. Oxford university press, USA.

Grams PE, Topping DJ, Schmidt JC, Hazel JE, Kaplinski M. 2013. Linking morphodynamic response with sediment mass balance on the Colorado River in Marble Canyon: issues of scale, geomorphic setting, and sampling design. *Journal of Geophysical Research-Earth Surface* 118: 361–381.

Guzman C, Tilahun S, Zegeye A, Steenhuis T. 2013. Suspended sediment concentration – discharge relationships in the (sub-) humid Ethiopian highlands. *Hydrology & Earth System Sciences* 17: 1067–1077.

Hartley AJ, Weissmann GS, Nichols GJ, Warwick GL. 2010. Large distributive fluvial system: characteristics, distribution and controls on development. *Journal of Sedimentary Research* 80: 167–183.

Hawkins P, Green P. 1993. Exploration results, hydrocarbon potential and future strategies for the northern Galilee Basin. *Australian Petroleum Exploration Association Journal* 33: 280–280.

Heller PL, Paola C. 1992. The large-scale dynamics of grain-size variation in alluvial basins, 2: application to syntectonic conglomerate. *Basin Research* 4: 91–102.

Hristopulos DT. 2003. Renormalization group methods in subsurface hydrology: overview and applications in hydraulic conductivity upscaling. *Advances in Water Resources* 26: 1279–1308.

Isaaks EH. 1984. Indicator simulation: application to the simulation of a high grade uranium mineralization. In: Geostatistics for natural resources characterization. Part 1.

Jiang Z, Mariethoz G, Farrell T, Schrank C, Cox M. 2015. Characterization of alluvial formation by stochastic modelling of paleo-fluvial processes: the concept and method. *Journal of Hydrology* 524: 367–377.

Jones AT, Fielding CR. 2008. Sedimentary facies of a glacially influenced continental succession in the Pennsylvanian Jericho Formation, Galilee Basin, Australia. *Sedimentology* 55: 531–556.

Journel AG, Huijbregts CJ. 1978. *Mining Geostatistics*. Academic press: London.

Koltermann CE, Gorelick SM. 1992. Paleoclimatic signature in terrestrial flood deposits. *Science* 256: 1775–1782.

Koltermann CE, Gorelick SM. 1996. Heterogeneity in sedimentary deposits: a review of structure-imitating, process-imitating, and descriptive approaches. *Water Resources Research* 32: 2617–2658.

Larned S, Hicks D, Schmidt J, Davey A, Dey K, Scarsbrook M, Arscott D, Woods R. 2008. The Selwyn River of New Zealand: a benchmark system for alluvial plain rivers. *River Research and Applications* 24: 1–21.

Le Méhauté B. 1976. *An Introduction to Hydrodynamics and Water Waves*. Springer-Verlag New York.

Lopez S, Cojan I, Rivoirard J, Galli A. 2009. Process-based stochastic modelling: meandering channelized reservoirs. *Analogue Numer Model Sediment System: From Understand Predict (Special Publ. 40 of the IAS)* 40: 139–144.

Lu S, Molz FJ, Fogg GE, Castle JW. 2002. Combining stochastic facies and fractal models for representing natural heterogeneity. *Hydrogeology Journal* 10: 475–482.

Mariethoz G, Lefebvre S. 2014. Bridges between multiple-point geostatistics and texture synthesis: review and guidelines for future research. *Computers & Geosciences* 66: 66–80.

Michael H, Li H, Boucher A, Sun T, Caers J, Gorelick S. 2010. Combining geologic-process models and geostatistics for conditional simulation of 3-D subsurface heterogeneity. *Water Resources Research* 46: W05527.

Morin RH. 2005. Hydrologic properties of coal beds in the Powder River Basin, Montana I. Geophysical log analysis. *Journal of Hydrology* 308: 227–241.

Paola C, Heller PL, Angevine CL. 1992. The large-scale dynamics of grain-size variation in alluvial basins, 1: theory. *Basin Research* 4: 73–90.

Paola C, Voller V. 2005. A generalized Exner equation for sediment mass balance. *Journal of Geophysical Research: Earth Surface (2003–2012)* 110: F04014.

Remy N, Boucher A, Wu J. 2009. *Applied Geostatistics with SGeMS: A User's Guide*. Cambridge University Press, London.

Roscher M, Stordal F, Svensen H. 2011. The effect of global warming and global cooling on the distribution of the latest Permian climate zones. *Palaeogeography, Palaeoclimatology, Palaeoecology* 309: 186–200.

Soons JM, Moar NT, Shulmeister J, Wilson HD, Carter JA. 2002. Quaternary vegetation and climate changes on Banks Peninsula, South Island, New Zealand. *Global and Planetary Change* 33: 301–314.

Terry JP, Kostaschuk RA, Garimella S. 2006. Sediment deposition rate in the Falefa River basin, Upolu Island, Samoa. *Journal of Environmental Radioactivity* 86: 45–63.

Tetzlaff DM, Harbaugh JW. 1989. Simulating clastic sedimentation.

Timms W, Crane R, Anderson D, Bouzalakos S, Whelan M, McGeeney D, Rahman P, Guinea A, Acworth R. 2014. Vertical hydraulic conductivity of a clayey-silt aquitard: accelerated fluid flow in a centrifuge permeameter compared with *in situ* conditions. *Hydrology and Earth System Sciences Discussions* 11: 3155–3212.

Van Heeswijck A. 2010. Late Paleozoic to Early Mesozoic deformation in the northeastern Galilee Basin, Australia. *Australian Journal of Earth Sciences* 57: 431–451.

Vargas-Guzmán J, Al-Qassab H. 2006. Spatial conditional simulation of facies objects for modeling complex clastic reservoirs. *Journal of Petroleum Science and Engineering* 54: 1–9.

Vine RR. 1973. The Galilee Basin. *Bureau of Mineral Resources, Geology and Geophysics, Canberra*: 26.

Vine RR, Paine AGL. 1974. Hughenden Queensland, 1:250,000 geological series sheet SG/55-1, explanatory notes. *Bureau of Mineral Resources, Geology and Geophysics, Australia*: 38.

Webb EK, Anderson MP. 1996. Simulation of preferential flow in three-dimensional, heterogeneous conductivity fields with realistic internal architecture. *Water Resources Research* 32: 533–545.

Weissmann GS, Fogg GE. 1999. Multi-scale alluvial fan heterogeneity modeled with transition probability geostatistics in a sequence stratigraphic framework. *Journal of Hydrology* 226: 48–65.

Wilson D. 1985. Erosional and depositional trends in rivers of the Canterbury Plains, New Zealand. *Journal oí Hydrology (NZ) Vol* 24: 16–27.

Winter CL, Tartakovsky DM. 2002. Groundwater flow in heterogeneous composite aquifers. *Water Resources Research* 38: 2301–2311.

Zappa G, Bersezio R, Felletti F, Giudici M. 2006. Modeling heterogeneity of gravel-sand, braided stream, alluvial aquifers at the facies scale. *Journal of Hydrology* 325: 134–153.

Zinn B, Harvey CF. 2003. When good statistical models of aquifer heterogeneity go bad: a comparison of flow, dispersion, and mass transfer in connected and multivariate Gaussian hydraulic conductivity fields. *Water Resources Research* 39: 1051.